Nanostructures and flux pinning properties in YBa2Cu3O7−y thin films with double perovskite Ba2LuNbO6 nanorods

doi: https://doi.org/10.1063/5.0048693

Journal of Applied Physics

Nanostructures and flux pinning properties in $YBa_2Cu_3O_{7-y}$ thin films with double perovskite Ba_2LuNbO_6 nanorods

Masaya Gondo,[1] Masashi Yoshida,[1] Yuga Yoshida,[1] Manabu Ishimaru,[1,*] Tomoya Horide,[1] Kaname Matsumoto,[1] Ryusuke Kita[2]

[1]*Department of Materials Science and Engineering, Kyushu Institute of Technology, Kitakyushu, Fukuoka 804-8550, Japan*

[2]*Graduate School of Integrated Science and Technology, Shizuoka University, Hamamatsu, Shizuoka 432-8561, Japan*

Abstract

Double perovskite Ba_2LuNbO_6 (BLNO)-doped $YBa_2Cu_3O_{7-y}$ (YBCO) thin films are fabricated on a $SrTiO_3$ (001) substrate by pulsed laser deposition, and their nanostructures are characterized by transmission electron microscopy and scanning transmission electron microscopy. Cross-sectional observations and elemental mapping reveal that BLNO self-assembles during thin film deposition, and consequently, nanorods extending straight from the substrate to the surface are formed in the YBCO thin films. It is confirmed that stacking faults perpendicular to the growth direction disturb the formation of BLNO nanorods. Strain maps extracted by geometric phase analysis reveal that the tensile strain occurs in the YBCO matrix around the BLNO nanorods. Misfit dislocations are periodically introduced at the interface between the nanorod and matrix, which results in the inhomogeneous strain of YBCO around the BLNO nanorods. The superconducting properties of the YBCO+BLNO thin films are compared with those of other previously reported YBCO thin films with normal perovskite and double perovskite nanorods.

*To whom correspondence should be addressed. E-mail: ishimaru@post.matsc.kyutech.ac.jp

1. Introduction

The enhancement of the critical current density (J_c) of $REBa_2Cu_3O_{7-y}$ (REBCO: RE = rare earth, Nd, Sm, Gd, Y, and so forth) thin films is of technological importance for developing high-performance coated conductors. Because the migration of magnetic flux penetrating a superconductor gives rise to resistance, much effort has been devoted to introducing pinning centers, such as lattice defects, grain boundaries, and precipitates, to trap the magnetic flux [1-3]. $BaMO_3$ (BMO: M = Zr, Sn, Hf, and so forth), which has a perovskite-type structure, self-assembles during thin film deposition to result in the spontaneous formation of nanorods in the REBCO matrix [4-6]. The BMO nanorods act as pinning centers oriented along the *c*-axis of the REBCO thin films, which effectively improve J_c and the flux pinning force in a magnetic field applied parallel to the *c*-axis of the thin film.

The lattice parameter of BMO is different from that of REBCO, which causes strain at the interface between the matrix and nanorod [7-9]. The strain affects the physical properties of bulk and thin film superconductors [10-16], and therefore it is necessary to establish strain engineering for the development of novel coated conductors. However, the perovskite BMO nanorods introduced in the REBCO thin films are mainly $BHfO_3$, $BZrO_3$, and $BSnO_3$, and the selection of elements and compositions is limited. A double perovskite-type structure, represented as $A_2B'B''O_6$ (or $A'A''B_2O_6$), is attracting attention as a new artificial pinning center. In this structure, the sublattice of the B (A) sites of the normal perovskite-type structure (ABO_3) is regularly occupied by two different cations and the resultant structure possesses a unit cell that is twice that of ABO_3. The double perovskite structure has a higher degree of freedom in composition and lattice parameter than the conventional perovskite structure, which allows flexible control of the strain state. It has been confirmed that the superconducting characteristics in the applied magnetic field are improved by introducing nanorods with a

double perovskite structure [17-20].

The rare-earth elements can be introduced into one of the cation sites in the double perovskite structure, as seen in $Ba_2(Y,Nb)O_6$ [17,18] and $Ba(Y/Gd,Nb/Ta)O_6$ [21], and excess elements may precipitate as nanoparticles on the matrix or cause stacking faults. As a result, a hybrid pinning structure with a mixture of zero-, one-, and two-dimensional defects is spontaneously formed. It has been reported for REBCO+BMO thin films that the nanoparticles and stacking faults improve the J_c in a magnetic field applied parallel to the *ab*-plane of the thin film [22]. A similar improvement in the superconducting properties is anticipated in the double perovskite-doped REBCO films. This motivated us to synthesize double perovskite-doped REBCO thin films.

To control the superconducting properties, knowledge of the structures is required. However, the structural analysis of REBCO thin films containing double perovskite nanorods is relatively limited as compared with that of perovskite oxide BMO nanorods. In the present study, we prepare Ba_2LuNbO_6 (BLNO)-doped $YBa_2Cu_3O_{7-y}$ (YBCO) thin films by pulsed laser deposition and characterize their structures and strain state using transmission electron microscopy (TEM) and scanning transmission electron microscopy (STEM). As a result, it is observed that a hybrid pinning structure consisting of nanoparticles, nanorods, and stacking faults is spontaneously formed. The J_c characteristics of the YBCO+BLNO thin films are evaluated and the relationship with nanostructures is discussed.

2. Experimental

The YBCO+BLNO thin films with a thickness of ~160 nm were fabricated on a single-crystalline $SrTiO_3$ (STO) (001) substrate using pulsed laser deposition, where the mixed YBCO+BLNO (5 vol.%) targets were ablated. The oxygen partial pressure during the film

fabrication was 0.26 mbar and the laser frequency was 2 Hz. The growth temperature was 890 °C. The resistivity and J_c of the film were measured using a Quantum Design Physical Property Measurement System. Electric field strengths of 1 μV/cm and 10 μV/cm were used to define a magnetic field dependence of J_c and an angular dependence of J_c, respectively.

Cross-sectional specimens for TEM and STEM were prepared by mechanical polishing and Ar ion milling. Bright-field images and electron diffraction patterns were obtained by a JEOL JEM-3000F operated at 300 kV (Kyushu Institute of Technology). To estimate the lattice parameter from the electron diffraction pattern, the camera length was calibrated by the diffraction pattern of polycrystalline thallous chloride. Annular bright-field (ABF) and high-angle annular dark-field (HAADF) observations and elemental mapping were performed at an acceleration voltage of 200 kV using a JEOL JEM-ARM200CF equipped with dual silicon drift detectors of a 100 mm^2 sensor (Kyushu University). For the strain mapping, HAADF images were analyzed by DigitalMicrograph™ using a FRWR plugin from Humboldt-Universität zu Berlin [23].

3. Results and discussion

Figure 1(a) shows a cross-sectional bright-field TEM image of the YBCO+BLNO thin film grown on a STO substrate. The image was recorded a few degrees off the [010] zone axis of YBCO, where the 00*l*-type systematic reflection of YBCO was excited, so as to obtain a clear contrast. Moiré fringes caused by overlapping crystals with different lattice parameters were observed in the thin film. Because of the uniaxial excitation condition, the moiré fringes parallel to the YBCO/STO interface were emphasized. The difference in the direction of the moiré fringes between the right- and left-hand sides arose from the change in diffraction conditions caused by the slight bending of the TEM sample. In fact, the diffraction contrast of

the YBCO matrix was darker in the right region than that in the left. Most of the nanorods grew straight and continuously along the growth direction from the substrate, which indicated the formation of nanorods in the thin film. Figure 1(b) shows the electron diffraction pattern obtained from the thin film. In addition to the Bragg reflections of YBCO, weak spots arising from nanorods appeared, as marked by arrows. To interpret the experimental diffraction pattern, the structure factors were calculated on the basis of the kinematical approximation. The simulated pattern of Fig. 1(c) revealed that the arrangement of the extra spots was consistent with the (010) reciprocal lattice plane of BLNO with a double perovskite structure. (The 002 and its equivalent reflections of BLNO were too weak to detect.) From the electron diffraction patterns, the following orientation relationships were found to exist between the YBCO matrix and the BLNO nanorods: $(001)_{YBCO}//(001)_{BLNO}$ and $[010]_{YBCO}//[010]_{BLNO}$.

The lattice parameters of the BLNO nanorods were estimated to be 8.3(2) Å in the in-plane direction and 8.5(7) Å in the growth direction. (Because the spots of BLNO are spread in the diffraction pattern, the number at the second decimal place in parentheses contains an error.) That is, the BLNO nanorods embedded in the YBCO matrix were tetragonally distorted and the lattice parameter deviated from that of bulk BLNO (a = 8.368 Å [24]). When two lattices with the plane spacings d_1 and d_2 overlap in parallel, the interval of the moiré fringes, D, can be calculated by the following equation [25]:

$$D = \frac{d_1 d_2}{|d_1 - d_2|}.$$

Based on the spacing of the moiré fringes (36 Å) and the $(004)_{BLNO}$ planes along the growth direction, the spacing of the $(006)_{YBCO}$ planes was estimated to be 2.02 Å. The corresponding lattice parameter (c = 12.1(2) Å) was larger than that of the matrix (c = 11.67 Å) estimated from the electron diffraction pattern of Fig. 1(b), which suggested that the c-axis of YBCO was

elongated around the BLNO nanorod. In $BaZrO_3$-doped YBCO thin films, an average increase in the *c*-axis was observed with increasing $BaZrO_3$ concentration [7,26], which is consistent with the present results.

Figure 2(a) shows a cross-sectional ABF-STEM image of the YBCO+BLNO thin film. In addition to the nanorods, it was found that precipitates, as marked by arrows, were present in the thin film. Similar precipitates were also confirmed in Fig. 2(a), as marked by arrows. To identify the nanorods and precipitates, elemental mapping was performed using energy-dispersive X-ray spectroscopy (EDX). Figure 2(b–f) shows the EDX elemental maps taken by the characteristic X-rays of (b) Y-*L*, (c) Ba-*L*, (d) Cu-*K*, (e) Lu-*M*, and (f) Nb-*L*. The energy of the *M*-characteristic X-ray of Lu is 1.581 keV, which is within the energy range of soft X-rays (0.1–2 keV). Because the soft X-rays are easily absorbed by the specimen itself and/or by obstacles on the way to the detector, the results obtained here show only qualitative trends. The concentrations of Lu (Fig. 2(e)) and Nb (Fig. 2(f)) were high at the region of the moiré fringes elongated along the growth direction, which suggested that the BLNO nanorods were successfully formed in the specimen. The concentration of Ba was low, while that of Y was high in the precipitates. A precipitation of Y_2O_3 was observed in the $BaHfO_3$- [27] and $Ba_2Y(Nb,Ta)O_6$-doped YBCO thin films [19,20]. It should be noted that the Bragg spots corresponding to Y_2O_3 were not observed in the electron diffraction patterns which were taken from a wide area. Faint extra reflections were confirmed in fast Fourier transform (FFT) diagrams obtained from the precipitates (see Fig. S1 of the supplementary material), but the structure has not yet been determined. The precipitates were embedded in the YBCO matrix, and there was a possibility that the crystal structure was different from that of the equilibrium phase in the bulk state. Because of this, the precipitates observed here are called Y-rich precipitates.

To reveal the spatial distribution of nanorods, the cross-sectional ABF-STEM image taken from a wide area is shown in Fig. 3(a). The nanorods extended straight from the substrate to the surface of the thin film, but some of them were curved or interrupted in the middle of the thin film. It has been reported that the BMO nanorods grow thick and straight at high growth temperatures, while short, thin, and tilted nanorods are formed at low temperatures [28]. In the present study, the YBCO+BLNO thin film was deposited at 890 °C, and therefore, the factor that inhibited the formation of straight nanorods was not the growth temperature. Figure 3(b,c) shows magnified images of the areas enclosed by dashed squares in Fig. 3(a). A linear contrast perpendicular to the growth direction was observed in these images, which was attributed to the stacking fault located on the (001) plane of YBCO. The nanorods terminated by the stacking fault are shown in Fig. 3(b), while the nanorods curved at the stacking fault are observed in Fig. 3(c). However, several nanorods were uninterrupted at the stacking faults, as indicated by the arrows in Fig. 3(a). These results suggest that some of the stacking faults generated during the film deposition disturbed the growth of the nanorods.

Figure 4(a) shows a HAADF-STEM image of the YBCO+BLNO thin film on a STO substrate. The contrast of the HAADF image is proportional to the square of the atomic number, and therefore the STO substrate became dark. A BLNO nanorod existed at the dashed rectangular region. In fact, spots corresponding to BLNO were observed by Fourier transform of Fig. 4(a), as shown in Fig. 4(b), and the FFT diagram agreed with the electron diffraction pattern of Fig. 1(b). It was found that the positions of the spots corresponding to BLNO were slightly different between the electron diffraction pattern (Fig. 1(b)) and FFT diagram (Fig. 4(b)). This was proposed to arise from the thinning of the TEM specimen, but the qualitative trend in the lattice parameter change was still maintained.

Geometric phase analysis (GPA) [29,30] was employed to examine the spatial

distribution of strain. It is known that the precipitates and nanoparticles embedded in the matrix cause the moiré fringes which interfere with GPA [31]. Compared with the high-resolution TEM images, the moiré fringes were highly suppressed in the HAADF-STEM images. Indeed, the atomic arrangement of YBCO was clearly visible without moiré fringes, despite the overlap of YBCO and BLNO in the projection direction. Furthermore, we used the Fourier filtered image, which was extracted by choosing the YBCO spots only for GPA, to minimize the effects of the BLNO lattice and background noise on the strain map. The 003 and 100 spots of YBCO circled in Fig. 4(b) were used for the analysis. The radius of the mask for inverse FFT was set to be 0.4 nm^{-1}, which corresponded to a spatial resolution of 2.5 nm. An undistorted YBCO region (the left side of Fig. 4(a)), which contained neither defects nor nanorods, was chosen as the reference lattice. Figure 4 shows the resultant GPA strain maps for (c) the ε_{xx} and (d) ε_{yy} components, where the *x*- and *y*-axes are defined as the lateral and growth directions, respectively. It is apparent that the YBCO around the BLNO nanorod was subjected to tensile strain along the growth direction (Fig. 4(d)): the lattice parameter of YBCO became large around the BLNO nanorod. This result agrees with the moiré fringe analysis described above. However, the strain along the lateral direction (Fig. 4(c)) was almost negligible.

It should be noted that the strain distribution was not uniform. This inhomogeneous strain distribution was attributed to the existence of a misfit dislocation, which was periodically introduced at the interface between the YBCO matrix and the BLNO nanorod, as marked by arrows in Fig. 4(d). Feldmann *et al.* [17] found that Ba_2YNbO_6 nanorods embedded in YBCO are short segmented by the amorphous phase. Similar segmented Ba_2YNbO_6 nanorods were also observed by Wee *et al.* [18]. On the basis of the Lindemann criterion [32], it has been proposed that a solid-state amorphization is induced when the sum of the static and thermal mean-square displacements reaches a critical fraction of the interatomic spacing [33]. The

formation of nanorods segmented by the amorphous phase seems to occur at the high strain region owing to the lattice mismatch.

Maeda *et al.* [8] examined the strain field of $GdBa_2Cu_3O_{7-\delta}$ in the vicinity of the $BaHfO_3$ nanorods and found that the tensile strain fields locally extend to the matrix side. To examine the strain distribution at the interface, a magnified ε_{yy} strain map is shown in Fig. 4(e). Because the interface between the nanorod and the matrix was unclear in the HAADF image, the line connecting the misfit dislocations was assumed to be the interface. The tensile strain field extended in a semicircle toward the YBCO matrix side, as shown by the broken line. The line profile averaged at the solid rectangle in Fig. 4(d) is shown in Fig. 4(f). For comparison, the profile obtained from the matrix (dashed rectangle in Fig. 4(d)) is also indicated, where no strain exists. A maximum tensile strain of ~7% was observed in the region of the nanorod, and the amount of strain gradually decreased towards the interface. The tensile strain above the background noise still remained at the YBCO matrix, and the region extended up to ~3 nm, which is larger than the ~0.5 nm observed in $BaHfO_3$-doped $GdBa_2Cu_3O_{7-\delta}$ [8].

The interval of misfit dislocation was ~7 nm (Fig. 4(e)), which is longer than that observed in $BaZrO_3$-doped YBCO thin films (5.7 nm) [26]. Based on a mismatch of ~10% along the growth direction (8.5(7) Å (d_{002}=4.28 Å) for BLNO and 11.67 Å (d_{003}=3.88 Å) for YBCO), the interval of misfit dislocation was estimated to be ~4.2 nm, which is shorter than the experimental result (~7 nm). This suggests that the lattice mismatch at the interface between the BLNO nanorod and YBCO matrix was partially relaxed. There is a possibility that the strain changes around the nanorods affect the J_c in a magnetic field applied perpendicular to the *c*-axis of thin film. The lattice parameter of the double perovskite structure depends on the composition and the degree of cation ordering [34], and therefore the interval of the misfit dislocations and strain fields can be controlled by tuning the growth conditions of thin films.

For example, it seems possible to control the ratio of cations in the A- and/or B-sites of the double perovskite structure by changing the target composition.

Figure 5 shows the superconducting properties of the YBCO+BLNO thin film. From the resistance as a function of temperature (Fig. 5(a)), the critical temperature of the present specimen was estimated to be 89.5 K. Figure 5(b) shows the magnetic field (B) dependence of J_c at 77 K. A magnetic field was applied to the c-axis of the thin film. The J_c(0 T) and J_c(1 T) were 3.5 MA/cm^2 and 1.4 MA/cm^2, respectively. A J_c shoulder was observed at ~1.5 T, and J_c rapidly decreased with the increase in the magnetic field after exhibiting the shoulder, which suggested the matching field of ~1.5 T.

Figure 5(c) shows the pinning force (F_p) as a function of the magnetic field parallel to the c-axis. The F_p reached a maximum at 1.5 T. To examine the relationships between the structures and properties, plane-view TEM observations were performed (see Fig. S2 of the supplementary material). As a result, the average diameter and number density of BLNO nanorods were estimated to be ~11 nm and ~780 μm^{-2}, respectively. Because the matching field (B_Φ) is given by $n\phi_0$ (n: nanorod areal density, ϕ_0: magnetic flux quantum (2.07 × 10^{-15} Wb)), B_Φ was estimated to be 1.6 T for the present specimen. This value agrees with the magnetic field of the F_p peak (Fig. 5(c)) and the J_c shoulder (Fig. 5(b)), which suggested the matching field effect that is observed in other YBCO thin films containing nanorods. Rizzo *et al.* [35] reported that the nanorods have a mean diameter of ~5 nm and a density of ~2500 μm^{-2} in a YBCO+5 mol% Ba_2YTaO_6 film. Celentano *et al.* [20] demonstrated that $Ba_2Y(Nb,Ta)O_6$ (2.5 mol% Ba_2YNbO_6+2.5 mol% Ba_2YTaO_6) nanorods possess diameters of 12±2 nm and a density of ~540 μm^{-2}. On the basis of these results, it was proposed that the diameter of the BLNO nanorods can be controlled by tuning the growth conditions.

The angular (θ) dependence of J_c at a temperature of 77 K under B=2 and 5 T is

shown in Fig. 5(d). Although the J_c of the double perovskite-doped YBCO was measured under a magnetic field of 2 T, the value was larger than that of the YBCO with the conventional perovskite nanorods, $BaSnO_3$ and $BaHfO_3$ [22], under 1 T. The J_c had maximum values at 0° and 180°, which indicated that the BLNO nanorods effectively acted as a pinning center for the magnetic field parallel to the growth direction (B // c-axis direction of YBCO). A large c-axis peak in the J_c-θ curve was observed for $B \sim B_\Phi$, while the c-axis peak in the J_c-θ curve was small for $B > B_\Phi$. This confirmed the effective vortex pinning by the BLNO nanorods for $B < B_\Phi$.

Compared with the conventional perovskite nanorods, $BaHfO_3$ and $BaSnO_3$ [22], BLNO shows high J_c characteristics at 90°, parallel to the in-plane direction (B // ab-plane of YBCO). J_c(B//ab, 2 T) in YBCO+BLNO was larger than J_c(B//ab, 1 T) in YBCO+$BSnO_3$ with almost the same matching field (2 T), owing to the vortex pinning by Y-rich precipitates. This indicated self-organized hybrid pinning structure consisting of nanorods and nanoparticles. The J_c(B//ab, 2 T) was almost the same level as the J_c(B//ab) in other YBCO films containing double perovskite nanorods. The slight difference may originate from the morphologies of nanoprecipitates and other lattice defects such as stacking faults.

The comparison of the superconducting properties between the present and previous studies is summarized in Table 1. The $F_{p,max}$ was the same level as $F_{p,max}$ in YBCO+$BaSnO_3$ and YBCO+$BaHfO_3$, which indicated that the pinning efficiency of the BLNO nanorods was as large as that of the BMO nanorods. Although the nanorod structure was partially broken, as shown in the TEM image (Fig. 3), the decrease in the effective current flow area was not significant. The J_c of the YBCO+BLNO thin films under a magnetic field was larger than that of the YBCO thin films including conventional perovskite nanorods and was comparable to the double perovskite nanorods. These results suggest that the double perovskite BLNO nanorods become effective pinning centers, which is useful for developing higher performance coated

conductors.

4. Conclusions

We prepared BLNO-doped YBCO thin films by pulsed laser deposition, and examined their superconducting properties and atomistic structures. It was found that a hybrid pinning structure, which consists of Y-rich nanoparticles, BLNO nanorods, and stacking faults, is spontaneously formed during the film deposition. Cross-sectional observations reveal that most of the BLNO nanorods extend from the substrate to the surface, but some of them are terminated by the stacking fault generated during the deposition. The lattice parameter of the BLNO nanorods along the growth direction is larger than that along the in-plane direction, which results in the tetragonal distortion. Also, it was found that the *c*-axis of YBCO is extended around the BLNO nanorods. Misfit dislocations with an interval of ~7 nm are introduced at the interface between the nanorod and matrix, and the strain around the nanorod is partially relaxed. The strain maps obtained by GPA reveal that the inhomogeneous tensile strain generates around the BLNO nanorods owing to the periodically introduced misfit dislocations. It is also confirmed that the tensile strain fields are locally generated in the YBCO matrix near the BLNO nanorods. The YBCO+BLNO thin film exhibits the same level of $F_{p,max}$ as YBCO+$BaSnO_3$ and YBCO+$BaHfO_3$. The J_c of the YBCO+BLNO thin films under a magnetic field is larger than that of the YBCO thin films including conventional perovskite nanorods and comparable to the double perovskite nanorods.

Supplementary material

See supplementary material for the structure analysis of Y-rich precipitates (S1) and plane-view TEM observations of the YBCO+BLNO thin film (S2).

Acknowledgements

We acknowledge financial support by Japan Society for the Promotion of Science (JSPS) KAKENHI (Grant No. 18H01478). A part of this work was supported by "Advanced Characterization Nanotechnology Platform, Nanotechnology Platform Program of the Ministry of Education, Culture, Sports, Science and Technology (MEXT), Japan" at the Ultramicroscopy Research Center in Kyushu University (JPMXP09-A-19-KU-0034). We are grateful to Mr. Takaaki Toriyama of Kyushu University for his helpful support in transmission electron microscopy analysis. We thank Edanz Group (https://en-author-services.edanz.com/ac) for editing a draft of this manuscript.

Availability of data

The data that support the findings of this study are available within the article and its supplementary material.

References

[1] G. Blatter, M. V. Feigel'man, V. B. Geshkenbein, A. I. Larkin, and V. M. Vinokur, Rev. Mod. Phys. **66**, 1125 (1994).

[2] S. R. Foltyn, L. Civale, J. L. Macmanus-Driscoll, Q. X. Jia, B. Maiorov, H. Wang, and M. Maley, Nature Mater. **6**, 631 (2007).

[3] K. Matsumoto and P. Mele, Supercond. Sci. Technol. **23**, 014001 (2010).

[4] J. L. Macmanus-Driscoll, S. R. Foltyn, Q. X. Jia, H. Wang, A. Serquis, L. Civale, B. Maiorov, M. E. Hawley, M. P. Maley, and D. E. Peterson, Nature Mater. **3**, 439 (2004).

[5] Y. Yamada, K. Takahashi, H. Kobayashi, M. Konishi, T. Watanabe, A. Ibi, T. Muroga, S. Miyata, T. Kato, T. Hirayama, and Y. Shiohara, Appl. Phys. Lett. **87**, 132502 (2005).

[6] P. Mele, K. Matsumoto, T. Horide, A. Ichinose, M. Mukaida, Y. Yoshida, S. Horii, and R. Kita, Supercond. Sci. Technol. **21**, 032002 (2008).

[7] C. Cantoni, Y. Gao, S. H. Wee, E. D. Specht, J. Gazquez, J. Meng, S. J. Pennycook, and A. Goyal, ACS Nano **5**, 4783 (2011).

[8] T. Maeda, K. Kaneko. K. Yamada. A. Roy, Y. Sato, R. Teranishi, T. Kato, T. Izumi, and Y. Shiohara, Ultramicrosc. **176**, 151 (2017).

[9] T. Horide, M. Ishimaru, K. Sato, and K. Matsumoto, Phys. Rev. Mater. **3**, 013403 (2019).

[10] U. Welp, M. Grimsditch, S. Fleshler, W. Nessler, J. Downey, and G. W. Crabtree, Phys. Rev. Lett. **69**, 2130-2133 (1992).

[11] H. Sato and M. Naito, Physica C **274**, 221 (1997).

[12] N. Cheggour, J. W. Ekin, C. C. Clickner, D. T. Verebelyi, C. L. H. Thieme, R. Feenstra, and A. Goyal, Appl. Phys. Lett. **83**, 4223 (2003).

[13] M. Sugano, K. Osamura, W. Prusseit, R. Semerad, K. Itoh and T. Kiyoshi, Supercond. Sci. Technol. **18**, 369 (2005).

[14] F. Nabeshima, Y. Imai, M. Hanawa, I. Tsukada, and A. Maeda, Appl. Phys. Lett. **103**, 172602 (2013)

[15] S. Awaji, T. Suzuki, H. Oguro, K. Watanabe, and K. Matsumoto, Sci. Rep. **5**, 11156 (2015)

[16] K. Ahadi, L. Galletti, Y. Li, S. Salmani-Rezaie, W. Wu, and S. Stemmer, Sci. Adv. **5**, eaaw012 (2019).

[17] D. M. Feldmann, T. G. Holesinger, B. Maiorov, S. R. Foltyn, J. Y. Coulter, and I. Apodaca, Supercond. Sci. Technol. **23**, 095004 (2010).

[18] S. H. Wee, A. Goyal, Y. L. Zuev, C. Cantoni, V. Selvamanickam, and E. D. Specht, Appl. Phys. Express **3**, 023101 (2010).

[19] L. Opherden, M. Sieger, P. Pahlke, R. Hühne, L. Schultz, A. Meledin, G. Van Tendeloo, R. Nast, B. Holzapfel, M. Bianchetti, J. L. MacManus-Driscoll, and J. Hänisch, Sci. Rep. **6**, 21188 (2016).

[20] G. Celentano, F. Rizzo, A. Augieri, A. Mancini, V. Pinto, A. Rufoloni, A. Vannozzi, J. L. MacManus-Driscoll, J. Feighan, A. Kursumovic, A. Meledin, J. Mayer, and G. Van Tendeloo, Supercond. Sci. Technol. **33**, 044010 (2020).

[21] G. Ercolano, M. Bianchetti, S. C. Wimbush, S. A. Harrington, H. Wang, J. H. Lee, and J. L. MacManus-Driscoll, Supercond. Sci. Technol. **24**, 095012 (2011).

[22] T. Horide, N. Matsukida, M. Ishimaru, R. Kita, S. Awaji, and K. Matsumoto, Appl. Phys. Lett. **110**, 052601 (2017).

[23] https://www.physics.hu-berlin.de/en/sem/software/software_frwrtools (accessed February 11, 2021).

[24] A. A. Evdokimov and N. F. Men'shenina, Russ. J. Inorg. Chem. **27**, 1208 (1982).

[25] P. B. Hirsch, A. Howie, R. B. Pashley, and M. J. Whelan, Electron Microscopy of Thin

Crystals, London, Butterworthes (1965).

[26] T. Horide, F. Kametani, S. Yoshioka, T. Kitamura, and Kaname Matsumoto, ACS Nano **11**, 1780 (2017).

[27] T. Horide, K. Torigoe, M. Ishimaru, R. Kita, S. Awaji, and K. Matsumoto, Supercond. Sci. Technol. **33**, 105003 (2020).

[28] Y. Yoshida, S. Miura, Y. Tsuchiya, Y. Ichino, S. Awaji, K. Matsumoto, and A. Ichinose, Supercond. Sci. Technol. **30**, 104002 (2017).

[29] M. J. Hÿtch, E. Snoeck, and R. Kilaas, Ultramicrosc. **74**, 131 (1998).

[30] M. J. Hÿtch, J.-L. Putaux, and J.-M. Pénisson, Nature **423**, 270 (2003).

[31] Y. Wang and W. Zhang, Micron **125**, 102715 (2019).

[32] F. Lindemann, Z. Phys. **11**, 609 (1910).

[33] P. R. Okamoto, N. Q. Lam, and L. E. Rehn, Sol. Stat. Phys. **52**, 1 (1999).

[34] A. Masuno, M. Haruta, M. Azuma, H. Kurata, S. Isoda, M. Takano, and Y. Shimakawa, Appl. Phys. Lett. **89**, 211913 (2006).

[35] F. Rizzo, A. Augieri, A. Angrisani Armenio, V. Galluzzi, A. Mancini, V. Pinto, A. Rufoloni, A. Vannozzi, M. Bianchetti, A. Kursumovic, J. L. MacManus-Driscoll, A. Meledin, G. Van Tendeloo, and G. Celentano, APL Mater. **4**, 061101 (2016).

[36] P. Mele, K. Matsumoto, A. Ichinose, M. Mukaida, Y. Yoshida, S. Horii, and R. Kita, Supercond. Sci. Technol. **21**, 125017 (2008).

[37] G. Ercolano, M. Bianchetti, S.-L. Sahonta, A. Kursumovic, J. H. Lee, H. Wang, and J. L. MacManus-Driscoll, J. Appl. Phys. **116**, 033915 (2014).

Figure captions

Figure 1. (a) Cross-sectional bright-field TEM image of YBCO+BLNO thin film on a STO substrate. Gold on the surface is the electrode deposited for measuring the superconducting properties. In addition to BLNO nanorods, Y-rich precipitates, marked by arrows, exist in the thin film. The length of 10 moiré fringes is 36 nm. (b) Electron diffraction pattern taken from the thin film and (c) the corresponding simulated diffraction pattern. The intensity of the 002 spots of BLNO is too weak to detect.

Figure 2. (a) ABF-STEM image and (b–f) EDX elemental maps of YBCO+BLNO thin film. (b) Y-*L*, (c) Ba-*L*, (d) Cu-*K*, (e) Lu-*M*, and (f) Nb-*L*. In the ABF-STEM image, the contrast arising from the secondary phase is observed in the YBCO matrix. The concentration of Lu and Nb is high at the elongated contrast region, which suggests the formation of BLNO nanorods. However, Y-rich precipitates exist at the regions marked by arrows.

Figure 3. (a) ABF-STEM image taken from a wide area. Arrows indicate stacking faults on the (001) plane of YBCO. Nanorods extending from the substrate to the surface and nanorods interrupted in the middle of the thin film are observed in the image. (b, c) Magnified images of the regions surrounded by the dashed squares in (a). Stacking faults prevent the growth of the nanorods in (b), whereas they change the growth direction of the nanorods in (c).

Figure 4. (a) HAADF-STEM of YBCO thin film with a BLNO nanorod and (b) its Fourier power spectrum. A nanorod exists in the rectangle region. (c,d) GPA strain maps obtained from a Fourier filtered YBCO lattice image. (c) ε_{xx} and (d) ε_{yy} components, where the *x*- and *y*-axes are defined as the in-plane and growth directions, respectively. A remarkable tensile strain can

be seen at the nanorod. Misfit dislocations, some of them are marked by arrows in (d), are induced at the interface between the BLNO nanorod and YBCO matrix. (e) A magnified ε_{yy} strain map. A broken line denotes the tensile strain distribution at the YBCO matrix side. (f) The strain distribution around the nanorod (solid rectangle) and matrix (dashed rectangle) in (d). The strain distribution obtained from the dashed rectangle corresponds to the background noise. In the highlighted region on the YBCO matrix side near the BLNO, there is a significant tensile strain above the background.

Figure 5. (a) Resistivity of the YBCO+BLNO thin film as a function of temperature. The critical temperature is estimated to be 89.5 K. (b) The critical current density (J_c) under the magnetic field applied to the *c*-axis of the thin film at 77 K. A J_c shoulder is observed at ~1.5 T. (c) The pinning force (F_p) as a function of a magnetic field parallel to the *c*-axis. The F_p becomes a maximum at 1.5 T. (d) Angular dependence of the J_c at 77 K under a magnetic field of 2 and 5 T. The peak of J_c appears when the applied magnetic field is parallel to the *c*-axis (0° and 180°) and *ab*-plane (90°) of YBCO.

Table I. Comparison of the superconducting properties of YBCO thin films containing normal perovskite and double perovskite nanorods. T_c: critical temperature; B_Φ: matching field; $F_{p,max}$: maximum pinning force, J_c: critical current density under a magnetic field parallel to the *c*-axis and *ab*-plane of YBCO.

	Fraction	T_c (K)	B_Φ (T)	$F_{P,max}$ (GN/m^3) (@77 K)	J_c (MA/cm^2) (B // c @77 K)	J_c (MA/cm^2) (B // ab @77 K)
Ba_2LuNbO_3[A]	5 vol.%	89.5	1.5	17.5 (1.5 T)	0.76 (2 T)	0.45 (2 T)
$BaHfO_3$[B]	3.1 vol.%	89.0	2.6	15.9 (3 T)	0.61 (1 T)	0.34 (1 T)
$BaSnO_3$[C]	4 vol.%	88.6	4.8	28.3 (2 T)	0.38 (5 T)	-
$BaSnO_3$[B]	5.4 vol.%	89.6	2.0	13.4 (2 T)	0.64 (1 T)	0.27 (1 T)
Ba_2YNbO_6[D]	5 mol% BNO + 5 mol% Y_2O_3	92.0-92.5	1.4-1.7	32.3 (2.5 T) (75.5 K)	2.03 (1 T)	0.59 (1 T)
$Ba_2Y(Nb/Ta)O_6$[E]	2.5 mol% BYNO + 2.5 mol% BYTO	90.5-90.8	1.6-2.3	21.5 (1.7 T)-25.0 (2.3 T)	1.08-1.18 (2T)	0.37-0.51 (2 T)
Ba_2YNbO_6[F]	5 mol%	88-89	1.3-2.0	6 (1.3-1.4 T)	0.44-0.62 (1 T)	0.21-0.57 (1 T)
Ba_2YTaO_6[G]	5 mol% BYTO	-	5.2	9.1 (3 T)	0.56 (1 T)	0.69 (1 T)
$Ba_2Y(Nb/Ta)O_6$[G]	2.5 mol% BYNO + 2.5 mol% BYTO	-	5.2	11.5 (4.4 T)	0.51 (1 T)	0.51 (1 T)
Ba_2YNbO_6[H]	5.1 vol.%	88.3	-	-	0.66 (1 T)	0.33 (1 T)

A: Present work, B: Ref. 22, C: Ref. 36, D: Ref. 17, E: Ref. 19 , F: Ref. 37, G: Ref. 35, H: Ref. 18

AIP Publishing

Journal of Applied Physics

ACCEPTED MANUSCRIPT

PLEASE CITE THIS ARTICLE AS DOI: 10.1063/5.0048693

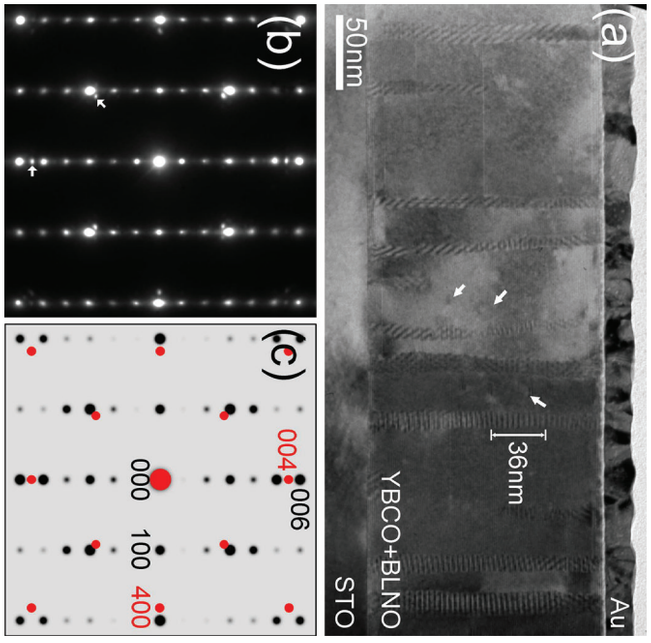

AIP Publishing

Journal of Applied Physics

ACCEPTED MANUSCRIPT

PLEASE CITE THIS ARTICLE AS DOI: 10.1063/5.0048698

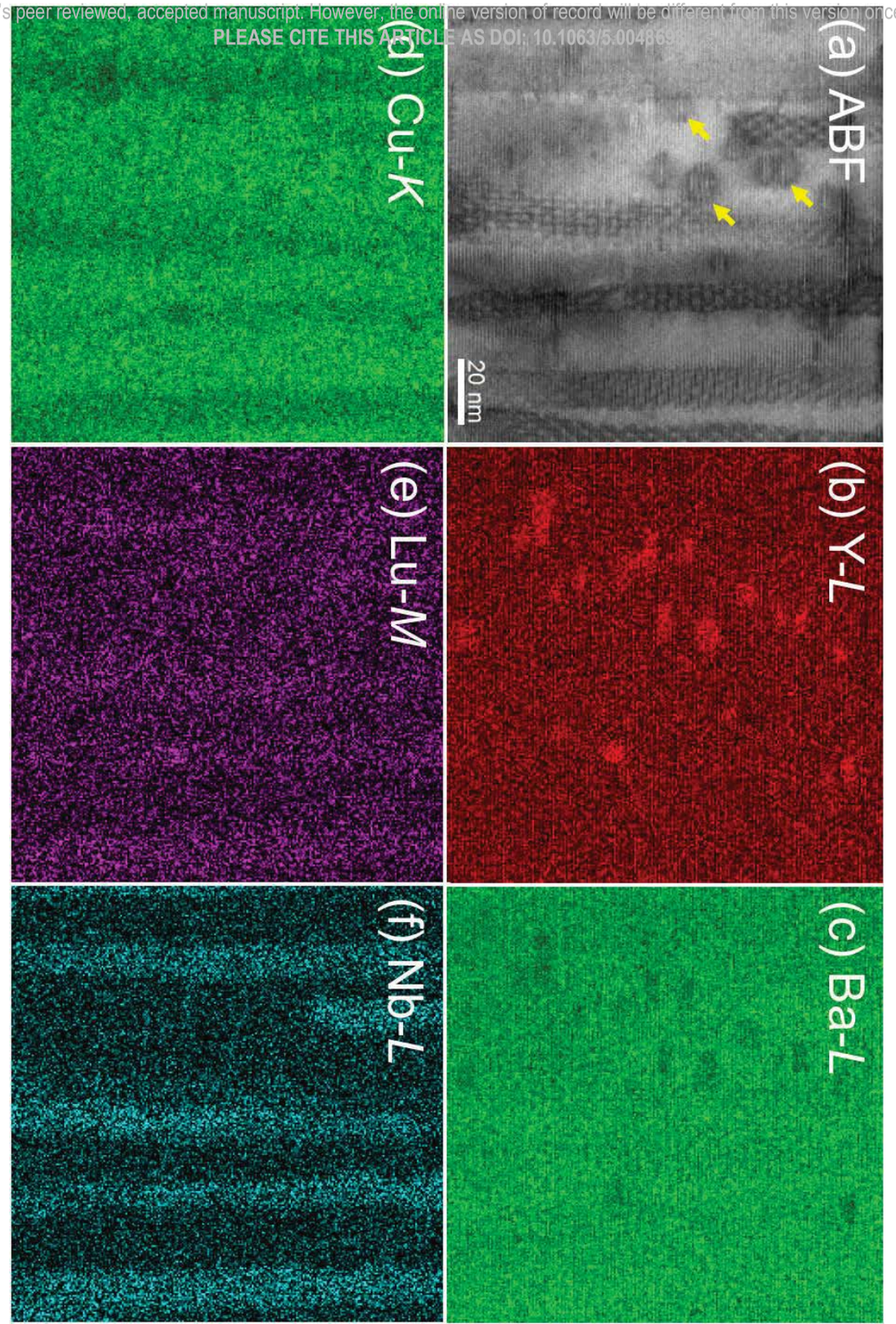

AIP Publishing

Journal of Applied Physics

ACCEPTED MANUSCRIPT

PLEASE CITE THIS ARTICLE AS DOI: 10.1063/5.0048693

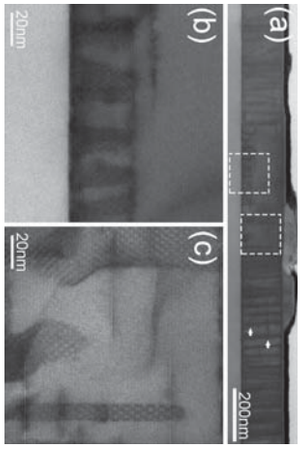

AIP Publishing

Journal of Applied Physics

ACCEPTED MANUSCRIPT

PLEASE CITE THIS ARTICLE AS DOI: 10.1063/5.0048693

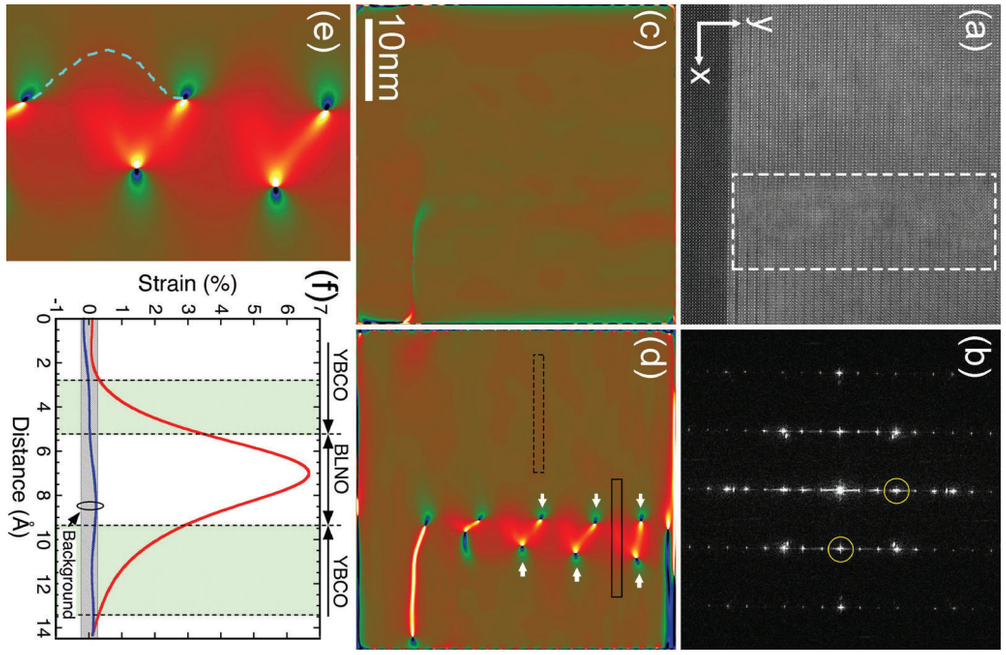

Journal of Applied Physics